INTERNATIONAL JOURNAL OF CLIMATOLOGY
Int. J. Climatol. (2011)
Published online in Wiley Online Library
(wileyonlinelibrary.com) DOI: 10.1002/joc.2303

RMetS
Royal Meteorological Society

Observational and supportive modelling analyses of winter precipitation change in China over the last half century

Robert R. Gillies,[a,b]* Shih-Yu Wang[a,b] and Wan-Ru Huang[c]
[a] *Utah Climate Center, Utah State University, Logan, UT, USA*
[b] *Department of Plants, Soils, and Climate, Utah State University, Logan, UT, USA*
[c] *Guy Carpenter Asia-Pacific Climate Impact Centre, City University of Hong Kong, Hong Kong, China*

ABSTRACT: Overall increasing trends in annual precipitation and widespread warming over China have been documented. During the winter months in southeast China, where snow is commonplace but rarely accumulates, the climatological 0 °C surface isotherm generally defines the southern boundary of the snowfield. Therefore, a warming climate will: (a) modify the southern boundary of the snowfield; and (b) potentially alter the snow-rain ratio. Using recently released daily precipitation from the Asian Precipitation-Highly Resolved Observational Data Integration Towards Evaluation (APHRODITE) and temperature observations from the ERA-40/Interim Reanalyses, this study investigated historical winter precipitation changes in China. Since snowfall observations were largely unavailable for southeast China, snowfall amounts were estimated using a rain-snow threshold temperature (RST) method which was subsequently verified by *in situ* and satellite observations of snow depth, snow cover, and snow water equivalent (SWE). The composite analysis reveals a decrease in snowfall totals which are accompanied by an increase in rainfall; this change corresponds with the northward retreat of the 0 °C surface isotherm and the snow-rain ratio. Atmospheric circulation analysis indicated lower tropospheric warming with increased moisture over southeast China, consistent with previous studies. Moreover, we observed an increase in the convergence of water vapour flux which sustains the increase in precipitation; this is accompanied by the suppression of snowfall due to the lower tropospheric warming. An additional analysis employed to further substantiate the RST method was undertaken by modelling the snow-rain ratio with the Weather Research and Forecasting (WRF) Model. The results were in agreement with those estimated from the observations. Copyright © 2011 Royal Meteorological Society

KEY WORDS climate change; precipitation regime; snowfall; China

Received 9 August 2010; Revised 13 January 2011; Accepted 17 January 2011

1. Introduction

The number of climate change studies focusing on China has grown rapidly since the release of the third Assessment Report of the IPCC (IPCC, 2001). Numerous studies (Hu *et al*., 2003; Gemmer *et al*., 2004; Wang *et al*., 2004; Wang and Zhou, 2005; Zhai *et al*., 2005; Su *et al*., 2006; Becker *et al*., 2006; Zhou and Yu, 2006; Qian and Qin, 2008) have reported upon mixed trends in annual precipitation over the last half century accompanied with a widespread temperature increase at the surface. Particularly over southern and eastern (SE) China – which is defined as the area south of 40°N with the topography below 1000 metres (cf. Fig. 1(b)), and where the majority of the nation's population dwell – observed trends in winter precipitation are uniformly positive. The increasing precipitation has been accompanied by decreasing surface evaporation (Thomas, 2000; Gao *et al*., 2006) and increasing lower-tropospheric temperatures (Guo and Ding, 2009). These winter features are different from observed trends in summer precipitation which exhibit a localised, north-south stratified pattern across the Yangtze River (Gemmer *et al*., 2004; Zhai *et al*., 2005), proposed to be associated with changes in the onset and length of the Meiyu season (Becker *et al*., 2006).

Winter precipitation in SE China (Figure 1(a)) is mainly distributed south of the climatological 0 °C isotherm at the surface (near 35°N; Figure 1(b)). The concurrence between the precipitation and the 0 °C isotherm implies the occurrence of snowfall. However, unlike mountainous regions in which snow accumulates above the snowline and is stored as snowpack, snowfall in SE China hardly ever accumulates for an extensive length of time. As indicated by the long-term snow cover extent observed from the Advanced Very High Resolution Radiometer (AVHRR) (Figure 1(a)), SE China – with less than 10% of winter snow cover extent – is considered to be climatologically snow free. Nonetheless, winter snowfall is not uncommon in provinces south of the Yangzi River (∼30 °N), especially when East Asian cold surges advance southward bringing in cold dry air from Siberia to encounter warm moist air originating from the coast (Chang *et al*., 1983; Chan and Li, 2004). A particularly profound example of the mixing of two such distinct air masses occurred in January 2008 when SE China

* Correspondence to: Dr. Robert R. Gillies, Utah Climate Center, Utah State University, 4825 Old Main Hill, Logan, UT 84322-4825.
E-mail: Robert.Gillies@usu.edu

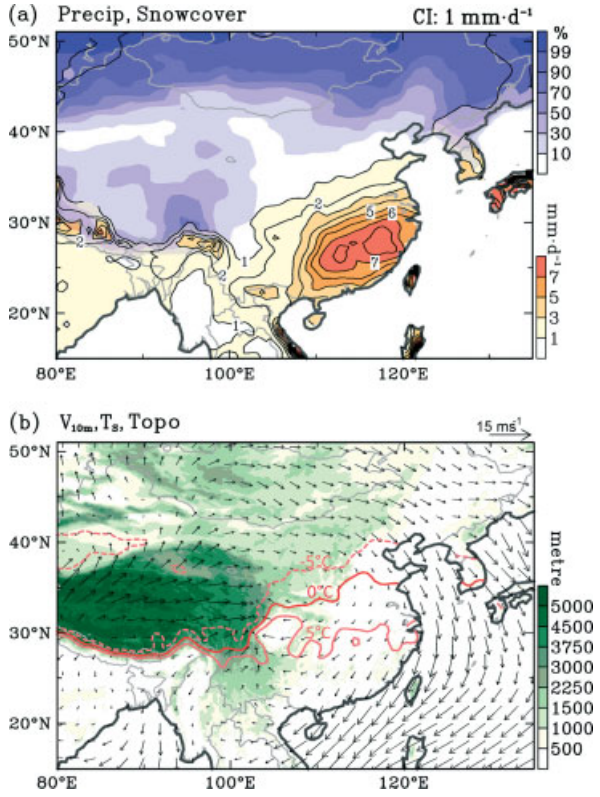

Figure 1. (a) Precipitation (filled contours; contour interval 1 mm d^{-1}) and AVHRR snow cover extent, and (b) topography (shadings) superimposed with 10-metre wind vectors and 2-metre temperature (contours; only plotted for −5 °C, 0 °C, and 5 °C) for the December–February climatology.

underwent the heaviest snow event in decades (Wen *et al*., 2009), resulting in over 100 casualties and affecting nearly 80 million people across 14 provinces – including 5 that are south of the Yangzi River. What is unclear to date, however, is whether this isolated extreme snow event was perhaps linked to the documented climate change in the region.

The effect of global warming on snowpack and snowmelt has been studied extensively. A review by Stewart (2009) showed that declining snowpack and earlier snowmelt are occurring in the major mountain regions around the world as warmer temperatures decrease snowpack and cause an earlier spring melt-off. The shift in temperature conditions considerably affects water availability in snow-dominated regions (Barnett *et al*., 2005), while the hydrological regime has shifted such that even in regions that reveal an increasing trend in precipitation, they too are similarly affected by a warming trend (Stewart, 2009). Persistent warming also affects the position of the 0 °C isotherm at the surface and thereby modifies the spatial extent of the winter precipitation regime (consisting of snowfall and rainfall) (Bonsal and Prowse, 2003). Over SE China where tall mountain ranges are absent and snow does not last for long on the ground, changes in the precipitation regime may reflect the migration of the 0 °C isotherm coupled with any associated climate change.

In this paper, we investigate such a scenario in an attempt to verify and quantify any changes in the winter precipitation regime. The first challenge for such a task was the sparseness of direct snowfall observations in SE China. Thus, we utilised a newly released daily precipitation dataset for Asia; this is introduced in Section 2. Results in the climatology and trends of winter precipitation regime are presented in Section 3. Circulation aspects associated with the trends, are highlighted and discussed in Section 4. A regional numerical simulation was also carried out and the analysis is contained in Section 5. Section 6 summarises our findings and provides some conclusions.

2. Data and methodology

2.1. Data resources

A new gridded daily precipitation dataset, compiled by the Asian Precipitation-Highly Resolved Observational Data Integration Towards Evaluation of the Water Resources (APHRODITE's Water Resources; Xie *et al*., 2007), was released in May 2009 on the APHRODITE's Water Resources project webpage http://www.chikyu.ac.jp/precip/. The APHRODITE dataset was compiled through a cooperative effort by the Research Institute for Humanity and Nature and the Meteorological Research Institute of Japan. The APHRODITE precipitation data were derived from rain gauges throughout monsoon Asia, including China, Mongolia and Indochina; the spatial and temporal resolution is respectively 0.5° long. x 0.5° lat. (about 50 km) from 1961 to 2004. The APHRODITE dataset, therefore, provides an unprecedented coverage of fine-resolution daily precipitation data across East and Southeast Asia. For verification purposes, a limited set of daily temperature, precipitation and snow depth records for Chinese stations, as part of the WMO World Weather Watch Program, were compared with the analysis of the APHRODITE data. These station records cover the time period from 1973 to 2008, but only about one quarter of the stations contained snow depth observations.

Surface and upper-air meteorological variables were obtained from the 1.25°-resolution ERA40 global reanalyses (Uppala *et al*., 2005) generated by the European Centre for Medium-Range Weather Forecasts (ECMWF) and were provided by the National Center for Atmospheric Research's Mass Storage System. The ERA40 is a three-dimensional variational data assimilation (3DVAR) system derived from the ECMWF operational Integrated Forecast Model. The model is spectral semi-Lagrangian with a resolution of triangular truncation 159 (T159) with 60 levels in the vertical. The assimilation system includes terrestrial observations of temperature, pressure, wind and humidity together with a significant quantity of satellite observations. The ERA40 reanalyses provided estimates of daily two-metre mean air temperatures (T_{2m}) that were assimilated from surface temperature observations. Since the ERA40 reanalyses were only available up to 2002, for years 2003 and beyond we used the newer ERA-Interim (ERAI) reanalyses that cover the period from 1989 to the present (Uppala *et al*., 2008) with a T255 resolution.

However, for data uniformity we reduced the resolutions for both the ERAI and the APHRODITE data to 1.25° using bilinear interpolation.

The assimilated T_{2m} combined with the observed precipitation made it possible to come up with an estimate of daily snowfall over each 1.25° grid cell using a climatological approach, which is introduced in Section 2.2. As a verification of this method, we utilised daily snow water equivalent (SWE) retrieved from passive microwave measurements taken by the Advanced Microwave Scanning Radiometer-Earth Observing System (AMSR-E); this data was available from 2002 to the present at the National Snow and Ice Data Center (NSIDC; http://nsidc.org). For details of the SWE retrieval algorithm, see Kelly *et al.* (2005). In addition, daily and monthly snow cover extent (available 1972–the present) observed from the AVHRR were included in our analysis. The AVHRR snow and ice observations were obtained from the Ice Mapping System at the National Ice Center (NIC-IMS; Ramsay, 1998) at http://www.natice.noaa.gov/ims/.

2.2. Rain-Snow Temperature – background and rationale

Climatological estimates of snowfall may be obtained by using the Rain-Snow Temperature method (RST) using the T_{2m}. Early experiments conducted by the United States Army Corps of Engineers (1956) suggested that an air temperature of 2 °C was a reasonable dividing point that defines precipitation falling as either rain or snow. Later, Auer (1974) analysed T_{2m} along with measurements of solid and liquid precipitation over 1000 weather stations and found that, at around a $T_{2m} = 2.5$ °C, the probability of finding rain and snow were equal. Further, Auer reported that for $T_{2m} < 0$ °C precipitation was virtually all snow, and for $T_{2m} > 6.1$ °C precipitation was all rain. Adopting Auer's results, Yang *et al.* (1997) used a single RST = 2.2 °C for climate model data and found this temperature to be reasonable and effective in separating rain from snow. Later studies (e.g. Yuter *et al.*, 2006; Lundquist *et al.*, 2008; Jones, 2010) used a 1 °C wet-bulb temperature with a transition of −1 °C/+1 °C, respectively, to separate mixed phases of snow and rain. There is a general agreement given in these studies that $T_{2m} = 0$ °C roughly marks the transition that defines all snow to mixed-phase precipitation, while $T_{2m} = 2$ °C marks the transition point from mixed-phase to all rain. Therefore, at $T_{2m} = 1$ °C, a mixed precipitation type would contain about half snow and half rain (Lundquist *et al.*, 2008; Jones, 2010). Motoyama (1990) estimated the RST in Japan and obtained values of 0 °C for a cold region (Hokkaido, ∼45 °N) and 1–3 °C for a relatively warm region (Honshu, 35°–40°N) for T_{2m} to define mixed precipitation type of snow and rain.

Given the warmer climate of SE China and its geographic approximation with Japan, we decided to adopt Motoyama's (1990) experimental result of $0\,°C \le T_{2m} \le 2\,°C$ for the RST method. At each 1.25° × 1.25° grid cell, a RST = 1 °C means that the grid-scale precipitation would be categorised fully as snow at $T_{2m} \le 0$ °C, and fully as rain at $T_{2m} \ge 2$ °C, while in between the range there would be half snow and half rain. However, we also included two additional settings of RST: RST = 0 °C ($-1\,°C \le T_{2m} \le 1\,°C$) and RST = 2 °C ($1\,°C \le T_{2m} \le 3\,°C$) in order to assess any inherent sensitivities that might affect our results and conclusions.

2.3. Verification of the RST method

It should be noted that most of the aforementioned studies using the RST method focused on high-latitude and/or high-elevation regions where the air humidity is presumably lower than that of Monsoon Asia. However, the lack of an observational network to directly measure snowfall in SE China makes it impossible to quantitatively evaluate the selected RST values. As a justification of our RST categories, we analysed several snow events along with available satellite observations. A randomly selected snow event in SE China on 5–7 December 2002 is shown in Figure 2. Precipitation occurred on 5 December along the southern edge of a cold air outbreak (∼30 °N; Figure 2(a)). On this day, the 0 °C isotherm was positioned north of 35°N, and precipitation occurred mainly as rainfall; here, snowfall was estimated from the APHRODITE data using RST = 1 °C (i.e. $0\,°C \le T_{2m} \le 2\,°C$). On 6 December (Figure 2(b)), the 0 °C isotherm had moved southward to 30°N, following the advance of the cold air outbreak, and had generated snowfall over an extensive area (indicated by a dashed circle). Meanwhile, the 500-hPa wind fields and 700-hPa wet-bulb temperatures (T_W; Figure 2(d) and (e)) show that the precipitation occurred to the east of a shortwave trough located near 110 °E. Two days later on 8 December (Figure 2(c)), the cold surge broke southward pushing the 0 °C isotherm and precipitation towards the southern coast as the trough deepened substantially (Figure 2(f)). Such shortwave troughs and associated frontal precipitation are typical precursors to the East Asian cold surges (Cheang, 1987; Chen *et al.*, 1999; Chan and Li, 2004). Of note, however, is the latitudinal position of the 0 °C wet-bulb isotherm at 700 hPa, which essentially coincides with the surface 0 °C isotherms; this feature reflects the shallow structure of East Asian cold surges where density currents intrude equatorward underneath the mid-tropospheric air (Chang *et al.*, 1983; Chen *et al.*, 1999). Such shallow structure implies freezing temperatures being uniformly distributed throughout the lower troposphere, which indicates a weakly saturated adiabatic lapse rate, in which case snow falling toward the ground is less likely to melt.

Verification of the estimated snowfall was conducted by computing the SWE difference (observed from the AMSR-E) between the 6–7 December and 4–5 December averages (Figure 2(g); we adopted this two-day average to fill in the gap between daily swaps of the satellite (e.g. Figure 3(b)). Caution should be taken here as the amounts of differential SWE cannot be directly compared with the amounts of snowfall, since changes in SWE

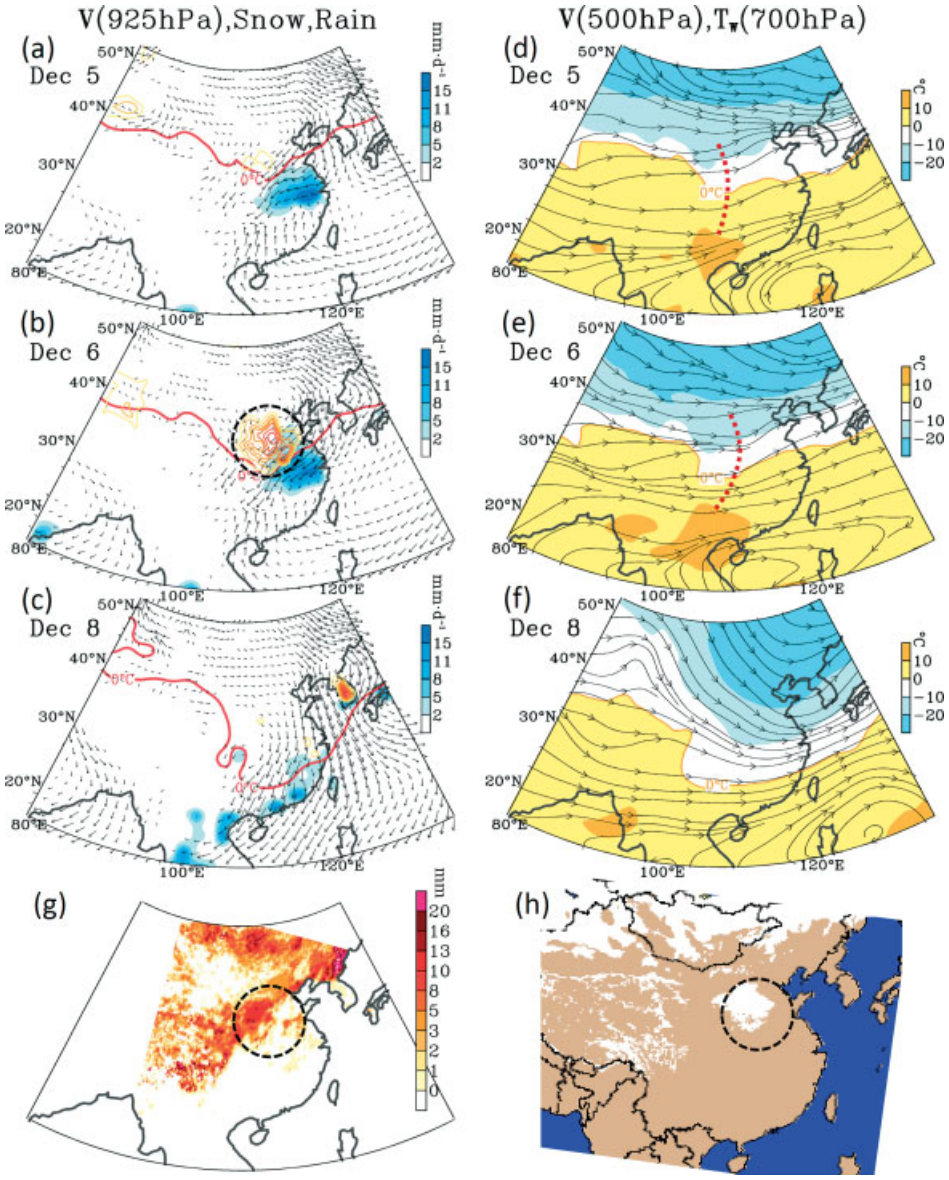

Figure 2. Estimated (from RST method) daily mean rainfall (shadings) and snowfall (contours; contour interval 2 mm/d) superimposed with the 0 °C isotherm of T_{2m} (thick red contours) and the 925-hPa wind vectors on 5 December (a); 6 (b); and 8 (c), 2002. The corresponding 500-hPa streamlines and 700-hPa web-bulb temperature (shadings) are shown in (d)–(f). (g) Difference in SWE between 6–7 December and 4–5 December. (h) AVHRR snow extent on 7 December (white areas). Dashed circles in (b), (g) and (h) indicate the snow area described in the text. Red dotted lines in (d) and (e) indicate the short-wave trough.

involve more than one parameter such as air temperature, humidity and pressure changes, all of which influence snow depth and water content (Lundquist *et al.*, 2008). Nevertheless, during the event, there was an apparent increase in SWE around 112 °E and 37°N (Figure 2(g); circled) which is in good agreement with the snowfall's distribution (Figure 2(b)). Also noticeable, are scattered areas of SWE over the Tibetan Plateau and north of 40°N, likely resulting from diurnal variations of temperature and humidity. Moreover, the AVHRR snow cover extent on 7 December (Figure 2(h)), a day after the major snowfall, reveals a consistent area that was covered with snow (circled), which further affirms the snowfall estimate and observed increase in SWE.

Two additional random cases are presented in Figure 3: On 22 December 2002, snowfall occurred over central-eastern China associated with a cold air outbreak (Figure 3(a)). Further to the analysis conducted earlier, the snowfall estimate is consistent with: (i) positive differential SWE between 20–21 and 22–23 December (Figure 3(b)); and (ii) the AVHRR snow cover extent observation of the following day (23 December; Figure 3(c)). The other event occurred on 11 February 2003 (Figure 3(d)) and snowfall was captured further south near 30°N along the southern edge of a strong cold air outbreak. The patterns of differential SWE (Figure 3(e)) and snow cover extent (Figure 3(f)) again confirm the southward advance of snowfall. The

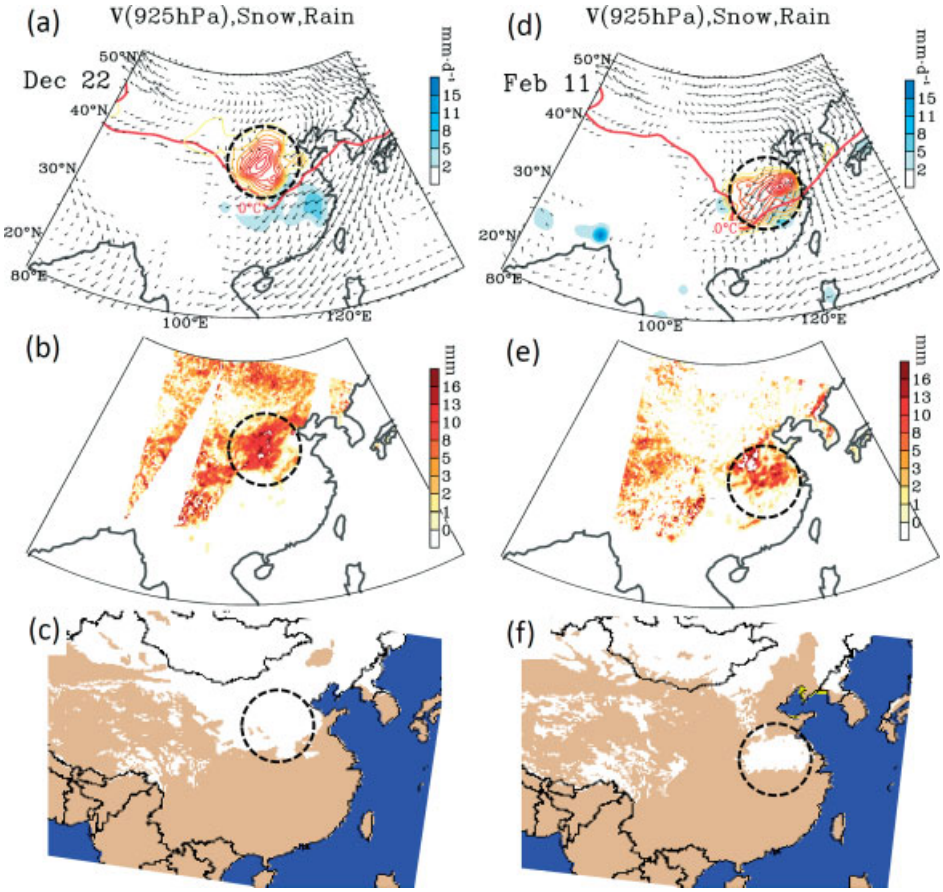

Figure 3. (a)–(c) Same as Figure 2(c), (d) and (h) except for the case on 22 December 2002. (d)–(f) Same as (a)–(c) but for the case on 11 February 2003.

marked agreements between estimated snowfall and satellite observations of SWE and snow cover extent in these three cases instill a certain degree of confidence in the RST method for SE China.

3. Climatology and trends

A winter precipitation regime comprising snowfall and rainfall can be described by the ratio between snowfall (S) and total precipitation (P), expressed as a percentage (hereafter, S/P). The horizontal distribution of climatological S/P, computed with the three RST settings of 0, 1, and 2 °C during the winters (DJF) of 1961–2004, is given in Figure 4(a); these depict a pattern similar to the snow cover extent climatology (Figure 1(a)) but depart somewhat in its southern extent into SE China. The RST settings manifest slight fluctuations of the S/P ratio over SE China between the −5 and 5 °C isotherms. The spatial distribution of snowfall estimates (Figure 4(b)) shows a 'snow band' across SE China (25–35°N). The amount and coverage of this snow band both increase at higher RST settings: At RST = 2 °C (i.e. 1 °C ≤ T_{2m} ≤ 3 °C), substantial snowfall covers part of the Guangdong and Guangxi provinces (∼110 °E, 25°N), but this is likely an overestimate since those two provinces experience a subtropical climate and hence, rarely receive snow. Large snowfall amounts are present over the southwestern Tibetan Plateau and along the northeastern Asian coast, whereas central and western China are distinctly dry in terms of snowfall despite a large S/P; these are also consistent with the climatology of snow cover extent (Figure 1(a)). The spatial distribution of the linear trends in S/P (Figure 4(c)) depicts an area of robust decline with a rate of 20–30% per 40-year period over central-eastern China (enclosed by a box). Unlike the estimated S/P and snowfall, changes in the RST setting have little impact on the distribution and magnitude of the S/P trends. This suggests that the decline in S/P is an unassailable trend.

To verify the results derived from the APHRODITE dataset, station snow depth records averaged over the time period of 1973–2004 were superimposed on the estimated snowfall (Figure 4(b)). It was found that the snow band across SE China was spatially consistent with a series of stations that recorded snow depth. Additionally, we performed the same RST analysis, as for Figure 4, on the station temperature and precipitation data which are shown in Figure 5. To objectively compare the spatial patterns between Figures 4 and 5, station records were interpolated onto a 0.5° grid mesh using the Cressman (1959) scheme with radii of influence set at 0.5, 1, and 2°. A linear spatial correlation function was then applied as follows. By associating every grid cell i in SE China with a given variable F_i and denoting its variance

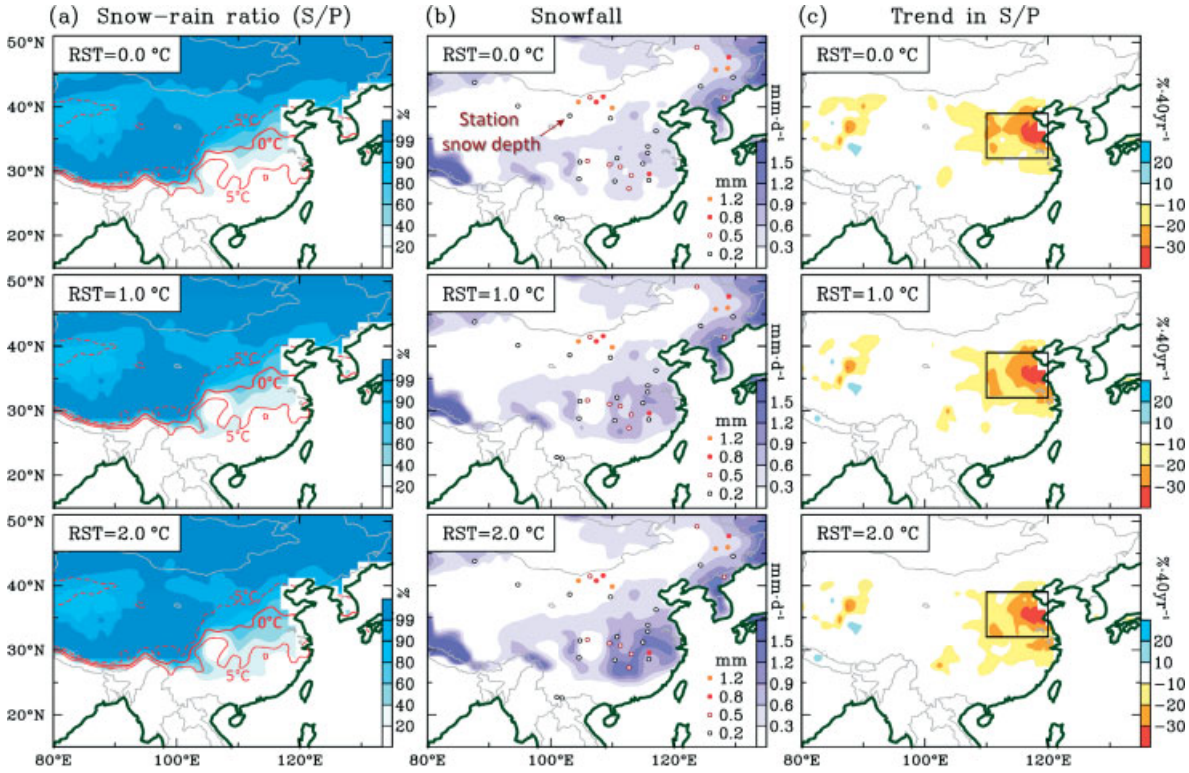

Figure 4. (a) Snowfall-precipitation ratio (S/P) in percentage, (b) estimated snowfall with station observations overlaid as colour dots (colour code given in the lower right), and (c) trends in S/P estimated from RST = 0 °C (top), 1 °C (middle), and 2 °C (bottom). The climatological isotherms of −5, 0 and 5 °C are plotted in (a) as red contours. Station snow depths (seasonal mean) are overlaid as dots and circles in (b).

as $\sigma_{F_i}^2$, then for F at two different grid cells i and j, the spatial correlation is given by $\rho_{i,j} \equiv \mathrm{cov}(F_i, F_j)/(\sigma_{F_i} \cdot \sigma_{F_j})$, where $\mathrm{cov}(F_i, F_j)$ is the covariance between F_i and F_j; this analysis yielded significant values of $\rho_{i,j}$ which are given in Figure 5, suggesting consistent patterns of S/P, snowfall, and S/P trends between stations and the reanalyses. The magnitudes of trends are also comparable between Figures 4 and 5.

The temporal evolution of the gridded S/P in the area with maximum declining trends (outlined in Figure 4(c)) was examined. As shown in Figure 6(a), the time series of S/P with RST = 1 °C is sandwiched between those of RST = 0 °C and 2 °C; this RST range results in an S/P fluctuation of about 15%. Regardless, all trends in Figure 6(a) are similarly significant with a decreasing rate of about 8.5% per decade after 1970. Previous studies (Xie *et al.*, 2005; Zhai *et al.*, 1999, 2005) pointed out that the increase in precipitation over SE China was associated with increases in both the precipitation frequency and daily precipitation extremes. Here, we examined the frequencies of precipitation and snowfall by counting the days when rainfall or snowfall at any grid point was greater than 0.5 mm·d^{-1} (i.e. a trace), based on RST = 1 °C. The precipitation frequency (Figure 6(b)) reveals an upward trend while the snowfall frequency shows a weak downward trend. The combination of these two opposite trends apparently leads to the marked decrease in S/P. Note also, that both the precipitation and snowfall frequencies undergo noticeable quasi-decadal oscillations, as are depicted by the 12-year low-passed snowfall time series in Figure 6(b). Similar low-frequency variations in precipitation have been noted and attributed to the inter-decadal variabilities of the regional-scale surface pressure anomalies (Xu and Chan, 2002) and the winter northeast Asian jet stream (Chang and Fu, 2002).

In the climatological perspective, precipitation variations generally follow the divergence of water vapour flux

$$\nabla \cdot \vec{\mathbf{Q}} = \nabla \cdot \left(\int_{p_S}^{300hPa} \vec{\mathbf{V}} q \cdot dp \right), \qquad (1)$$

where $\mathbf{V}$ denotes the horizontal wind, q is the specific humidity, p is the pressure level, and p_S is the surface pressure. For the same area as was defined in Figure 4(c), $\nabla \cdot \vec{\mathbf{Q}}$ features a marked downward trend (Figure 6(c)) indicating that, over time, the water vapour flux is converging and this supports the increasing precipitation. Zhai and Eskridge (1997) analysed radiosonde data in China and found that the atmospheric water vapour throughout SE China has undergone persistent increases in all seasons. In addition, Thomas (2000) reported that evapotranspiration in SE China has declined continually since the 1950s. Compiling these findings and neglecting the rate of change of precipitable water, the long-term balance of the water vapour budget equation can be approximated as

$$\nabla \cdot \vec{\mathbf{Q}} \approx E - P, \qquad (2)$$

where E is the evaporation/evapotranspiration and P is the precipitation. Thus, a downward trend in E and a

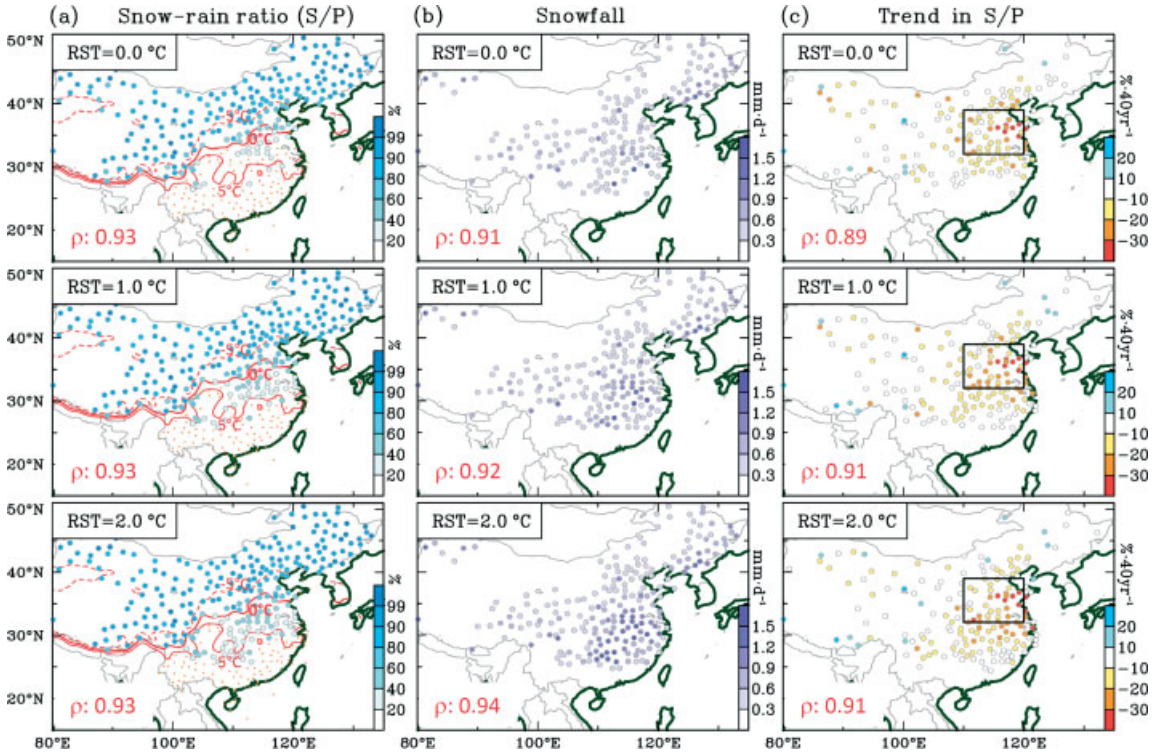

Figure 5. Same as Figure 4(a)–(c) except for station records during the time period of 1973–2008. Each dot denotes a station location. The colour scales correspond to those in Figure 4. Spatial correlation coefficients (ρ) of extrapolated patterns with Figure 4 (see text) are given in the lower left of each panel.

downward trend in $\nabla \cdot \vec{\mathbf{Q}}$ together should lead to an upward trend in P, and this suggests a hydrological explanation for the observed increase in winter precipitation throughout SE China.

Referring again to Figure 1, any temperature variation and change in SE China must accompany a positional shift of the 0 °C isotherm and, subsequently, the boundary that delineates the precipitation regime. This inference is substantiated in Figure 7 as the latitude-time Hovmöller diagrams of: (a) T_{2m}; (b) S/P; and (c) P, snowfall and snow cover, all averaged between 110 °E and 115 °E. Figure 7(a) is further evidence that the 0 °C isotherm has retreated northward about 1.5° in latitude over the period 1961–2004; this is consistent with the widely reported surface warming (cited earlier). Furthermore, it would be expected that there would be a similar response in the S/P ratio, as is evident in Figure 7(b) (RST = 1 °C). However, the northward shift in the S/P ratio is much more pronounced (nearly 2.5° in latitude) than that of T_{2m} (~1° in latitude). What is more, a distinct feature in its retreat is the rapidity to which this has occurred after the late 1980s. The monthly AVHRR snow cover extent confirms the northward retreat of the S/P ratio (Figure 7(c); green shadings); in this plot, it is clearly observed that, beginning in 1972, the southern boundary of the snow cover extent has shifted northward about 1° in latitude. The overall slower retreat of the snow cover extent at higher latitudes compared to the S/P ratio may be attributed to the colder climate where snow accumulation is less affected by surface warming (Stewart, 2009). These observations also correspond to the fact that the position of higher snow cover extent (>70%; Figure 7(c)) approximates the position of 100% S/P that remained stable until the 1990s (Figure 7(b)). However, and more importantly, the asymmetric rates of northward retreat between T_{2m} and S/P imply that additional forcing mechanisms other than surface warming are in place. These will be discussed in the next section.

The rainfall and snowfall estimates over the 44-year period are shown in Figure 7(c). Although a clear declining tendency in snowfall is evident, which matches with Figure 6(b), there is no apparent meridional position shift in the snowfall. On the other hand, rainfall has intensified notably in the last 20 years and has expanded northward about 1.5° in latitude, indicating that the increased winter precipitation is a combination of increased rainfall and decreased snowfall. Such a finding supports and quantifies one of the global warming scenarios predicting early melting snowpack, retreating snowlines and declining snowfalls (Barnett *et al.*, 2005).

4. Circulation anomalies

As noted previously, the increasing trends in winter precipitation over SE China have been widely reported, but the dynamic processes that have led to this occurrence have not been well documented. To facilitate the discussion, we decided to construct the differences in

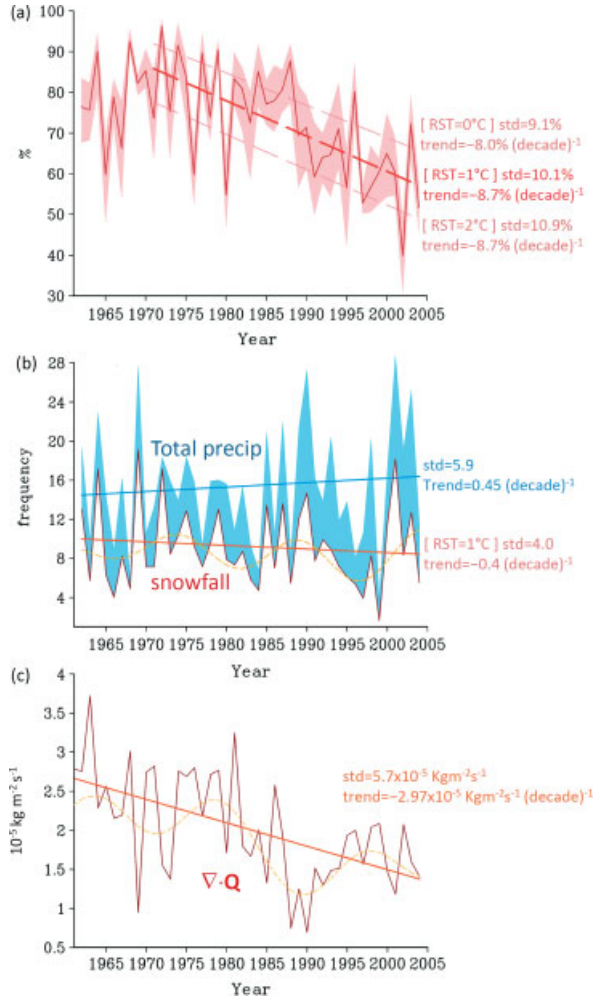

Figure 6. Time series of (a) S/P with RST = 1 °C (solid line) with the range between RST = 0 °C and 2 °C shaded in pink, (b) frequency of snowfall estimate (dark red curve) and total precipitation (blue shaded curve), and (c) divergence of water vapour flux averaged within a 5° × 5° domain as delineated in Figure 4(c). Trend and standard deviation (std) are given to the right of each least-square fitted lines. Low-frequency variations in (b) and (c) are indicated as yellow dashed curves filtered by a 12-year low-pass.

sea level pressure (Figure 8(a)) and 300-hPa geopotential height (Figure 8(b)) for the 1983–2004 period minus the 1961–1982 period. As is revealed in Figure 8(a), the prominent low-pressure anomalies over Mongolia reflect the rapid weakening of the Siberian high after the late 1970s as was reported by Panagiotopoulos *et al.* (2005) and Huang *et al.* (2010). Accompanying this weakening Siberian high, an anomalous anticyclone occurred in the upper troposphere over northeastern Asia (Figure 8(b)), indicating a decreased jet stream over northern China and consistent with Panagiotopoulos *et al.*'s analysis (cf. their Figure 8). In the mid-troposphere (Figure 8(c) and (d)), the differences in the geopotential height depict a synoptic-scale trough over Mongolia throughout central China (indicated by red dashed lines). This mid-tropospheric trough and the surface low pressure suggests a decrease in the strength of the East Asian winter monsoon (cf. Figure 1(b)), which is known to fluctuate in coherence with the Siberian high (Cheang, 1987; Chan and Li, 2004).

In their analysis of radiosonde data for SE China, Guo and Ding (2009) found a steady warming trend in the lower troposphere associated with a cooling trend in the upper troposphere. The lower tropospheric warming is in agreement with the southerly flow east of the synoptic-scale trough, as was inferred from Figure 8(d), since southerly flows in this region generally result in warm air advection. Given the preceding analysis, we then examined this from the perspective of the isobaric thermodynamic equation

$$\frac{\partial T}{\partial t} = -\mathbf{V}\cdot\nabla T + S\omega + \frac{J}{c_P}, \tag{3}$$

where

$$S = -\frac{RT}{p}\frac{d\ \ln\ \theta}{dp}.$$

Here, ω is the ERA40/ERAI vertical velocity, R is the dry-air gas constant, c_P is specific heat capacity for dry air at constant pressure, and J is the diabatic heating rate. The diabatic heating term $(-S\omega)$ is conventionally obtained from the residual of Equation (3) because diabatic heating in the reanalyses is generally considered to be model-biased. A diagnostic study by Honda *et al.* (1999) indicated that, over Asia in the mid-latitudes, Equation (3) for wintertime stationary waves in the troposphere can be approximated as a balance of

$$-\mathbf{V}\cdot\nabla T \approx -S\omega. \tag{4}$$

As indicated in Figure 8(c), decreases in adiabatic cooling covering eastern and SE China correspond well to increases in warm air advection (Figure 8(d)). Also noteworthy, is the fact that this area of strong warm advection covers where the maximum decline in the S/P ratio was observed (cf. Figure 4(c)). Furthermore, the anomalous trough in the mid-troposphere suggests that the frequency and/or the strength of synoptic shortwaves moving across central China (cf. Figure 2(f)) may be enhanced and, therefore, are more likely to form precipitation. However, these processes are less likely to produce snowfall due to the lower tropospheric warming.

At the large scale, vertical velocities are sustained dynamically through the divergent circulation. Thus, trends in the tropospheric divergent circulation were derived by computing the velocity potential at the 200 hPa (Figure 8(e)) and 850 hPa (Figure 8(f)) levels. What is revealed is that upper-level divergence (associated with a low-level convergence) over SE China indicates a vertically coupled divergent circulation that maintains ascending motion, which supports the upward trend in precipitation as well as the increase in $-S\omega$. Note that the 850-hPa convergence centre over Mongolia (Figure 8(f)) coincides with the weakening of the Siberian high (Figure 8(a)). However, the absence of any corresponding divergence centre at the upper levels suggests a tendency for shallow, dry upward motion – likely

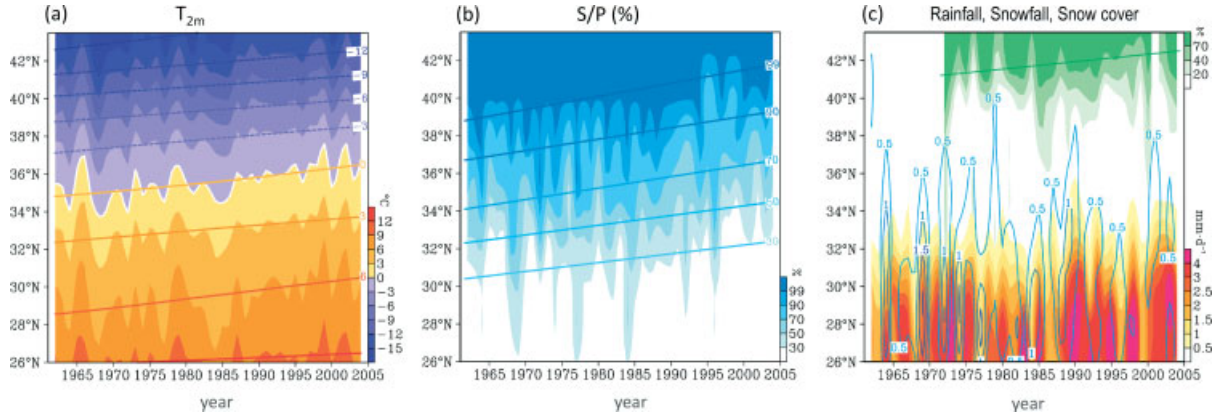

Figure 7. Latitude-time cross-sections averaged at 110–115 °E for (a) surface air temperature and (b) snowfall-precipitation ratio superimposed with their linear trends (lines), and (c) rainfall (orange shadings) and snowfall (blue contours) estimates superimposed with AVHRR snow cover observations (green shadings) with a trend line corresponding to 70% snow cover. All values are for the winter (December–February) mean.

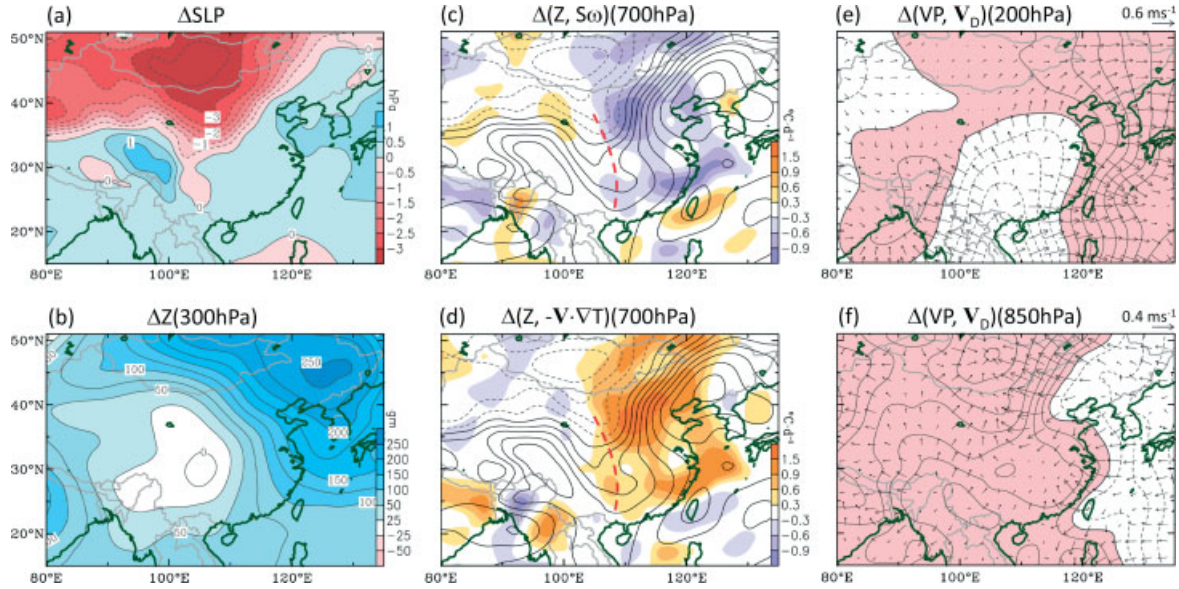

Figure 8. Differences (1983–2004 minus 1961–1982) of (a) sea level pressure (contour interval 0.5 hPa), (b) 300-hPa geopotential height (contour interval 25 m), 700-hPa geopotential height (contours; interval 10 m) with (c) adiabatic heating/cooling and (d) temperature advection (shadings), and velocity potential at 200 hPa (e) and 850 hPa (f) (contour interval 2×10^5 m^2 s^{-1}) with divergent wind vectors. Red dashed lines in (c) and (d) indicate the anomalous trough.

induced by the strong surface warming detected over Mongolia and Siberia (Dai, 2006; Zhou and Yu, 2006) where precipitation is low (cf. Figure 1(a)).

5. Regional climate simulation

The analysis of the S/P ratio presented thus far was a derivation from temperature and precipitation and while supported by complementary changes that have occurred in the atmosphere, these measurements may not be wholly convincing by themselves. To further substantiate our findings, we conducted a 30-year regional simulation (December 1979 – February 2009) using the Advanced Research version of the Weather Forecast and Research Model (WRF-ARW) (Dudhia, 2009). The WRF-ARW model was forced by boundary conditions derived from the National Centers for Environmental Prediction–Department of Energy Reanalyses II (Kanamitsu *et al*., 2002) and run at a 32 km horizontal resolution scale. Key model physics included the Betts-Miller-Janjic (BMJ; Betts, 1986; Betts and Miller, 1986; Janjic, 1994) cumulus parameterisation, a double-moment microphysics parameterisation introduced by Morrison *et al*. (2005), and the Mellor-Yamada-Janjic boundary layer parameterisation (Mellor and Yamada, 1982; Janjic, 2002). The simulation domain is outlined in Figure 9. Such a regional modelling approach, referred to as dynamical downscaling, has been widely used to reproduce high-resolution regional climate features in Europe (e.g. Christensen *et al*., 2007) and North America (Leung *et al*., 2006; Mearns *et al*., 2009; Wang *et al*., 2009). Here, we used SWE generated in the WRF-ARW to

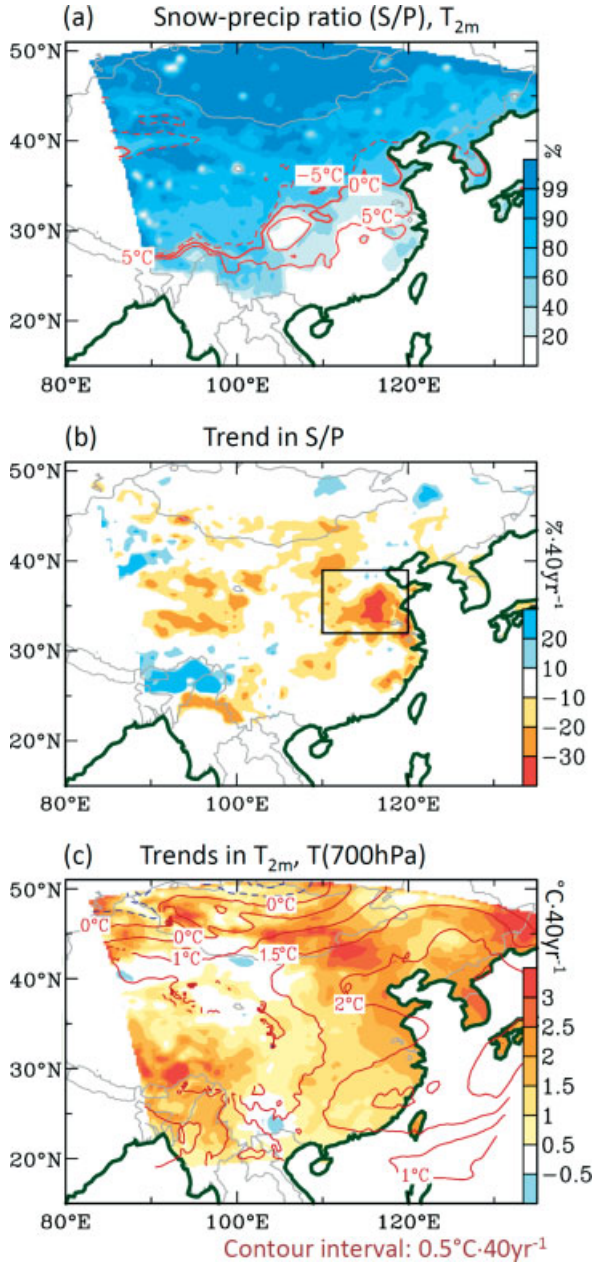

Figure 9. WRF-ARW simulations over the period 1979–2008 for (a) snowfall-precipitation ratio (S/P) superimposed with surface isotherms of −5, 0 and 5 °C, (b) trends in S/P derived from SWE, and (c) trends in T_{2m} (shadings) and 700-hPa temperature (contours).

estimate snowfall and S/P (computed as daily SWE divided by daily precipitation from 1 December through 28 February).

The simulated S/P ratio for the 30-year period is shown in Figure 9(a). Over SE China, the S/P ratio is generally 10% less than that estimated with RST = 1 °C (cf. Figure 4(a)), but their geographical distributions (and the simulated surface isotherms) are very consistent. The 10% decrease in the simulated S/P may occur partly because the use of SWE tends to underestimate the total snowfall, as snow can melt during the day and subsequently decrease any daily amounts of SWE. Such a possibility is supported by the generally consistent S/P percentages between the simulations and the observations at higher latitudes. In terms of trends in the S/P ratio (Figure 9(b)), the simulations are in good agreement with the observations and both indicate pronounced declines over central-eastern China (here, the simulated trends in the S/P ration were converted to 'per 40 years' to be comparable with Figure 4(c)). Furthermore, trends in the simulated T_{2m} (Figure 9(c)) point to a widespread warming in central and SE China accompanied by a substantial warming in northern China and Mongolia, all of which are consistent with those reported previously (e.g. Hu *et al.*, 2003; Zhou and Yu, 2006). In addition, the upward trend in the simulated 700-mb temperatures (Figure 9(c); contours) agrees well with the documented warmings at the surface and in the lower troposphere over eastern China. These results are consistent with, and are supportive of, the conclusion reached from the analysis in Figures 6–8.

A final question that remained was the unusual snow event of 2008, specifically, how did such an abnormal winter stand relative to the declining trend of S/P? We analysed the S/P ratio of January 2008 from station records with RST = 1 °C (Figure 10(a)), output from the ERAI (Figure 10(b)), and simulations of the WRF-ARW (Figure 10(c)). The results show that, over SE China, the average S/P estimated from all three methods lies between 20 and 60% (except for a few southern stations with S/P reaching 80%). Within the area covered by maximum decline in the S/P ratio (as outlined in Figure 9(b)), the average S/P in Figure 10 is 63% for the stations, 61% for the ERAI, and 56% for the WRF-ARW which, when compared to Figure 6(a), is slightly above the projection of S/P at RST = 1 °C but is under that at RST = 0 °C. In other words, although significant amounts of snowfall occurred in January 2008, proportionally larger amounts of rainfall were also produced. The circulation pattern of this particular winter consisted of an enhanced jet stream throughout the Middle East and a deepened trough over Tibet which brought in more moisture than normal (Wen *et al.*, 2009). Additionally, the abnormal winter of 2008 was more likely a result of a combined effect from different interannual climate modes (i.e. La Niña and strong Arctic oscillation), as was discussed in Wen *et al.* (2009), rather than as a result of the slowly changing atmospheric conditions.

6. Concluding remarks

During the past half century, winter precipitation and temperature in SE China have both undergone persistent upward trends. Because the area of winter precipitation overlaps with the climatological 0 °C isotherm at the surface, any changes in precipitation and temperature may result in changes in snowfall. Using the APHRODITE precipitation data, the ERA40/I reanalyses, and available *in situ* data, this study investigated observed changes in the winter precipitation regime over China for the last half century. The results indicate a

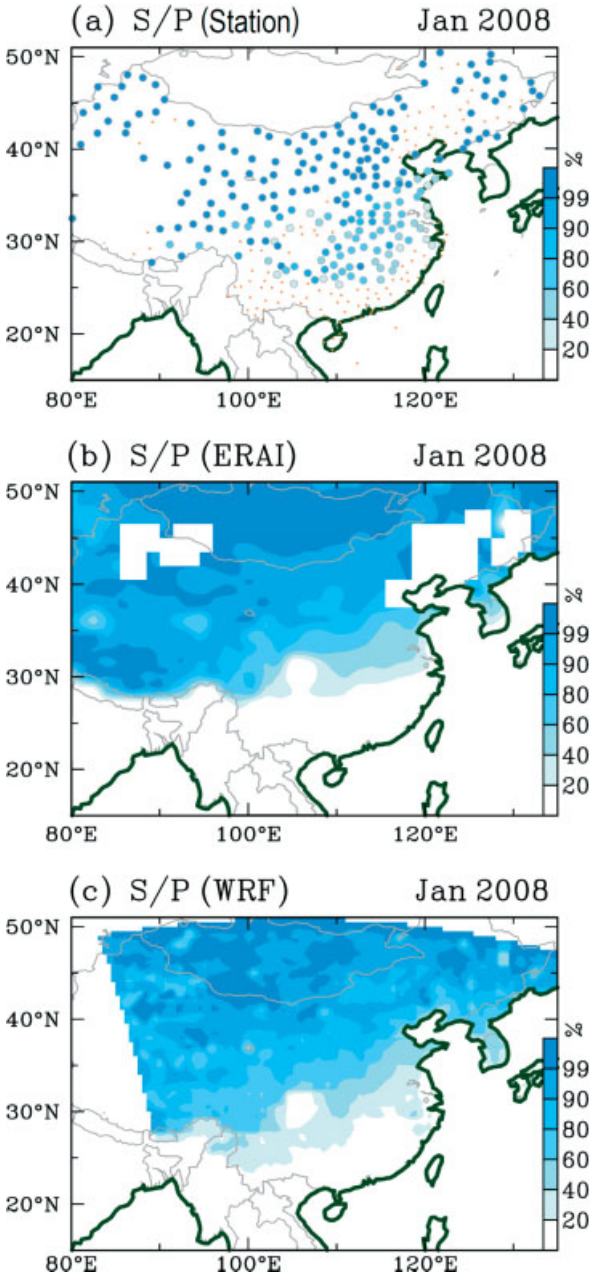

Figure 10. S/P in January 2008 derived from (a) stations with RST = 1 °C, (b) ERAI with model snowfall and precipitation, and (c) WRF-ARW simulations of SWE and precipitation. In (a) orange dots indicate stations that either received zero precipitation or S/P is under 20%. Blank grid cells in (b) are due to zero or extremely low precipitation in the ERAI.

decrease in snowfall associated with an increase in rainfall over much of SE China, leading to a drastic decline in the S/P ratio in central-eastern China. Analyses of the atmospheric circulation confirm previous findings of a warming lower troposphere along with increased moisture and decreased evapotranspiration in SE China. Together, these features formed a pronounced increase in the convergence of water vapour flux that sustained the precipitation increase, while a prominent warming in the lower troposphere reduced the occurrence of snow. The substantial warming that has occurred both at the surface and below 700 hPa (~2 °C in 40 years) over the climatological 0 °C isotherm region are manifest by changes in the direction of both reduced snowfall and increased rainfall. Moreover, a dynamical downscaling analysis using the WRF-ARM over the analysis area corresponded well with the observational analysis.

The results presented here are loosely quantitative as snowfall was not directly measured, being estimated from the RST method using daily precipitation and T_{2m} and by WRF-ARM simulations. The microphysical processes leading to any changes in snowfall in a warming climate requires further analysis. Nevertheless, substantial agreements in the various trends of moisture, precipitation, tropospheric circulation, and the heat budget signify an inevitable decline in snowfall and S/P over SE China. These results support the climate change scenario of declining snowfall as reported around the globe (Barnett *et al*., 2005). Furthermore, the rapidly declining strength of the Siberian high and its associated global teleconnection (Panagiotopoulos *et al*., 2005) may play an essential role in forming the widespread tropospheric warming and moistening over this region which, subsequently, may have sped up the S/P decrease. The combined effect of increasing precipitation (and frequency) and decreasing S/P suggests an increased chance for extreme winter precipitation events in SE China. Numerical assessments of such a decline for the future using current version climate models would provide helpful insights as to what degree the snow climatology of monsoon Asia will change.

Acknowledgements

This study was supported by the USDA-CSREES-funded Drought Management, Utah Project, and approved by the Utah Agricultural Experiment Station, Utah State University, as journal paper number 8275.

References

Auer AH. 1974. The rain versus snow threshold temperatures. *Weatherwise* **27**: 67.

Barnett TP, Adam JC, Lettenmaier DP. 2005. Potential impacts of a warming climate on water availability in snow-dominated regions. *Nature* **438**: 303–309.

Becker S, Gemmer M, Jiang T. 2006. Spatiotemporal analysis of precipitation trends in the Yangtze River catchment. *Stochiastic Environmental Research and Risk Assessment* **20**: 435–444.

Betts AK. 1986. A new convective adjustment scheme. Part I: Observational and theoretical basis. *Quarterly Journal of the Royal Meteorological Society* **112**: 677–691.

Betts AK, Miller MJ. 1986. A new convective adjustment scheme. Part II: Single-column tests using GATE wave, BOMEX, ATEX and Arctic air-mass data sets. *Quarterly Journal of the Royal Meteorological Society* **112**: 693–709.

Bonsal B R, Prowse T D. 2003. Trends and variability in spring and autumn 0 °C-isothermdates over Canada. *Climatic Change* **57**: 341–358.

Chan JCL, Li C. 2004. The East Asia winter monsoon. In *East Asian Monsoon*, Chang CP, (ed). World Scientific: Singapore; pp. 54–106.

Chang C-P, Millard J, Chen G. 1983. Gravitational character of cold surges during Winter MONEX. *Monthly Weather Review* **111**: 293–307.

Chang EKM, Fu Y. 2002. Interdecadal variations in Northern Hemisphere winter storm track intensity. *Journal of Climate* **15**: 642–658.

Cheang B-K. 1987. Short- and long-range monsoon prediction in Southeast Asia. In *Monsoons*, Fein JS, Stephens PL, (eds), John Wiley and Sons: New York; 579–619.

Chen T-C, Yen M-C, Wang S-Y, Arritt RW. 1999. Roll clouds associated with an East Asian cold front. *Bulletin of the American Meteorological Society* **80**: 2199–2208.

Christensen JH, Carter TR, Rummukainen M, Amanatidis G. 2007. Evaluating the performance and utility of regional climate models: the PRUDENCE project. *Climate Dynamics* **81**: 1–6.

Cressman GP. 1959. An operational analysis system. *Monthly Weather Review* **87**: 367–374.

Dai A. 2006. Recent climatology, variability, and trends in global surface humidity. *Journal of Climate* **19**: 3589–3606.

Dudhia J. 2009. WRF Version3.1: New features and updates. 10th WRF Users' Workshop, Boulder, CO, June 23–26, 2009 (available at http://www.mmm.ucar.edu/wrf/users/workshops/WS2009/presentations/1-01.pdf).

Gao G, Chen D, Ren G, Chen Y, Liao Y. 2006. Spatial and temporal variations and controlling factors of potential evapotranspiration in China: 1956–2000. *Journal of Geographical Sciences* **16**: 3–12.

Gemmer M, Becker S, Jiang T. 2004. Observed monthly precipitation trends in China 1951–2002. *Theoretical and Applied Climatology* **77**: 39–45.

Guo Y, Ding Y. 2009. Long-term free-atmosphere temperature trends in China derived from homogenized in situ radiosonde temperature series. *Journal of Climate* **22**: 1037–1051.

Honda M, Yamazaki K, Nakamura H, Takeuchi K. 1999. Dynamic and thermodynamic characteristics of atmospheric response to anomalous sea-ice extent in the Sea of Okhotsk. *Journal of Climate* **12**: 3347–3358.

Hu Z-Z, Yang S, Wu R. 2003. Long-term climate variations in China and global warming signals. *Journal of Geophysical Research* **108**(D19): 4614, DOI:10.1029/2003JD003651.

Huang W-R, Wang S-Y, Chan LC-L. 2010. Discrepancies between global reanalyses and observations in the interdecadal variations of Southeast Asian cold surge. *International Journal of Climatology* (in press), DOI:10.1002/joc.2234.

IPCC (Intergovernmental Panel on Climate Change). 2001. *Climate change 2001: The scientific basis*, Cambridge: Cambridge University Press: pp. 785.

Janjic ZI. 1994. The step-mountain eta coordinate model: Further developments of the convection, viscous sublayer, and turbulence closure schemes. *Monthly Weather Review* **122**: 927–945.

2002: Nonsingular implementation of the Mellor–Yamada level 2.5 scheme in the NCEP Meso-model. NCEP Office Note 437, NOAA/NWS, pp. 61.

Jones L P. 2010. Assessing the sensitivity of Wasatch snowfall to temperature variations. MS thesis, University of Utah.

Kanamitsu M, Ebisuzaki W, Woollen J, Yang S-K, Hnilo JJ, Fiorino M, Potter GL. 2002. NCEP–DOE AMIP-II Reanalysis (R-2). *Bulletin of the American Meteorological Society* **83**: 1631–1643.

Kelly REJ, Foster JL. 2005. The AMSR-E Snow Water Equivalent Product: Status and Future Development. Poster presented at the American Geophysical Union Fall Meeting, San Francisco, CA., 5–9 December 2005.

Leung LR, Kuo YH, Tribbia J. 2006. Research needs and directions of regional climate modeling using WRF and CCSM. *Bulletin of the American Meteorological Society* **87**: 1747–1751.

Lundquist JD, Neiman PJ, Martner B, White AB, Gottas DJ, Ralph FM. 2008. Rain versus snow in the Sierra Nevada, California: Comparing Doppler profiling radar and surface observations of melting Level. *Journal of Hydrometeorology* **9**: 194–211.

Mearns LO, Gutowski W, Jones R, Leung R, McGinnis S, Nunes A, Qian Y. 2009. North American Regional Climate Change Assessment Program: An overview. *EOS Transactions AGU* **90**(36): 311.

Mellor GL, Yamada T. 1982. Development of a turbulence closure model for geophysical fluid problems. *Reviews of Geophysics* **20**: 851–875.

Morrison H, Curry JA, Khvorostyanov VI. 2005. A new double-Moment microphysics parameterization for application in cloud and climate models. Part I: Description. *Journal of Atmospheric Science* **62**: 1665–1677.

Motoyama H. 1990. Simulation of seasonal snowcover based on air temperature and precipitation. *Journal of Applied Meteorology* **29**: 1104–1110.

Panagiotopoulos F, Shahgedanova M, Hannachi A, Stephenson DB. 2005. Observed trends and teleconnections of the Siberian High: A recently declining center of action. *Journal of Climate* **18**: 1411–1422.

Qian WH, Qin A. 2008. Precipitation division and climate shift in China from 1960 to 2000. *Theoretical and Applied Climatology* **93**: 1–17.

Ramsay BH. 1998. The interactive multisensor snow and ice mapping system. *Hydrological Processes* **12**: 1537–1546.

Su BD, Jiang T, Jin WB. 2006. Recent trends in observed temperature and precipitation extremes in the Yangtze River basin, China. *Theoretical and Applied Climatology* **83**: 139–151.

Stewart IT. 2009. Changes in snowpack and snowmelt runoff for key mountain regions. *Hydrological Processes* **23**: 78–94.

Thomas A. 2000. Spatial and temporal characteristics of potential evapotranspiration trends over China. *International Journal of Climatology* **20**: 381–396.

U.S. Army Corps of Engineers, 1956. *Snow Hydrology: Summary Report of the Snow Investigations*. Portland, OR: US Army Corps of Engineers, North Pacific Division.

Uppala SM, KÅllberg PW, Simmons AJ, Andrae U, Da Costa Bechtold V, Fiorino M, Gibson JK, Haseler J, Hernandez A, Kelly GA, Li X, Onogi K, Saarinen S, Sokka N, Allan RP, Andersson E, Arpe K, Balmaseda MA, Beljaars ACM, Van De Berg L, Bidlot J, Bormann N, Caires S, Chevallier1 F, Dethof1 A, Dragosavac M, Fisher M, Fuentes M, Hagemann S, Hólm E, Hoskins BJ, Isaksen L, Janssen PAEM, Jenne R, Mcnally AP, Mahfouf J-F, Morcrette J-J, Rayner NA, Saunders RW, Simon P, Sterl A, Trenberth KE, Untch A, Vasiljevic D, Viterbo P, Woollen J. 2005. The ERA-40 re-analysis. *Quarterly Journal of the Royal Meteorological Society* **131**: 2961–3012, DOI:10.1256/qj.04.176.

Uppala SM, Dee D, Kobayashi S, Berrisford P, Simmons A. 2008. Towards a climate data assimilation system: status update of ERA-Interim. *ECMWF Newsletter* **115**: 12–18 (http://www.ecmwf.int/publications/newsletters/pdf/115.pdf).

Wang S, Zhu J, Cai J. 2004. Interdecadal variability of temperature and precipitation in China since 1880. *Advances in Atmospheric Sciences* **21**: 307–313.

Wang S-Y, Gillies RR, Takle ES, Gutowski Jr WJ. 2009. Evaluation of precipitation in the Intermountain Region simulated by the NARCCAP regional climate models. *Geophysical Research Letters* **36**: L11704, DOI:10.1029/2009GL037930.

Wang Y, Zhou L. 2005. Observed trends in extreme precipitation events in China during 1961–2001 and the associated changes in large-scale circulation. *Geophysical Research Letters* **32**: L09707, DOI:10.1029/2005GL022574.

Wen M, Yang S, Kumar A, Zhang P. 2009. An analysis of the large-scale climate anomalies associated with the snowstorms affecting China in January 2008. *Monthly Weather Review* **137**: 1111–1131.

Xie P, Yatagai A, Chen M, Hayasaka T, Fukushima Y, Liu C, Yang S. 2007. A gauge-based analysis of daily precipitation over East Asia, *Journal of Hydrometeorology* **8**: 607–627.

Xie Z, Du Y, Jiang A, Ding Y. 2005. Climatic trends of different intensity heavy precipitation events concentration in China. *Journal of Geographical Sciences* **5**: 459–466.

Xu J, Chan JCL. 2002. Interannual and interdecadal variability of winter precipitation over China in relation to global sea level pressure anomalies. *Advances in Atmospheric Sciences* **19**: 914–926.

Yang Z-L. Dickinson RE, Robock A, Vinnikov KY. 1997. Validation of the snow submodel of the biosphere–atmosphere transfer scheme with Russian snow cover and meteorological observational data. *Journal of Climate* **10**: 353–373.

Yuter SE, Kingsmill DE, Nance LB, Löffler-Mang M. 2006. Observations of precipitation size and fall speed characteristics within coexisting rain and wet snow. *Journal of Applied Meteorology and Climatology* **45**: 1450–1464.

Zhai P, Eskridge RE. 1997. Atmospheric water vapor over China. *Journal of Climate* **10**: 2643–2652.

Zhai P, Sun A, Ren F, Liu X, Gao B, Zhang Q. 1999. Changes of climate extremes in China. *Climatic Change* **42**: 203–218.

Zhai P, Zhang X, Wan H, Pan X. 2005. Trends in total precipitation and frequency of daily precipitation extremes over China. *Journal of Climate* **18**: 1096–1108.

Zhou T, Yu R. 2006. Twentieth-century surface air temperature over China and the globe simulated by coupled climate models. *Journal of Climate* **19**: 5843–5858.

